*Journal of* ELECTRICAL ENGINEERING, VOL 73(2022), NO2, 152–157

sciendo

COMMUNICATIONS

# Investigation of field free region formed by dual Halbach array for focused magnetic hyperthermia

**Serhat Küçükdermenci**[1]

One of the challenges with magnetic fluid hyperthermia (MFH) is the limited control of magnetic nanoparticle (MNP) oscillations. To overcome this problem new approaches such as localization of MNP oscillations are being explored. In this study, we investigated the manipulation of field free region form by dual Halbach array displacements. We used finite element method simulation to examine gradient patterns in the workspace. Then, we created an experiment platform and took point probe measurements. As a result of the research, it was found that the field free region form can be manipulated by parametric distance changes of dual Halbach array. According to the findings, the field free region can expand and its shape can change from a point-like form to an ellipse-like surface by varying the distance between the arrays. The mapping of dual Halbach array generated gradient patterns for focused MFH was investigated for the first time in this study.

K e y w o r d s: cancer treatments, field free region, dual Halbach array, magnetic fluid hyperthermia, gradient pattern

## 1 Introduction

Conventional cancer treatments like ultrasound and microwave hyperthermia have relatively poor treatment outcomes and side effects. For example, in microwave hyperthermia the depth of penetration is poor and not suitable for the treatment of deep tumors. Although focusing abilities and depth of penetration are better, ultrasound therapy has the disadvantages of high energy absorption and reflection. RF probe hyperthermia has limited location sensitivity and poor access to deeply located tumors. An alternative approach to cancer treatments is magnetic fluid hyperthermia (MFH). MFH is a thermal therapy in which the temperature of cancerous cells are increased by the help of magnetic nanoparticles (MNPs). When nanoparticles MNPs are exposed to an alternating magnetic field (AMF) they cause an increase in the temperature of the tumor to which they are injected [1, 2]. This temperature $42-46\,^{\circ}\mathrm{C}$ can be used to destroy tumors, inhibit their growth or increase the susceptibility of tumors [3, 4]. Preclinical studies show that magnetic hyperthermia has significant potential to increase the sensitivity of cancer cells to radiation and chemotherapy or directly kill them [5, 6].

An applied AMF provides energy to change the orientation of the moments of MNPs. This moment movement that releases thermal energy is called the Nel relaxation mechanism [7] and depends on the anisotropy constant ($K$) and the volume of the particle ($V$). AMF can cause not only moment alignment but also the particle spin in the liquid medium. Such spin motion constitutes the Brownian mechanism, in which heating occurs in the surrounding carrier fluid. The Brownian relaxation time depends on the viscosity of the solution ($\eta$) and the hydrodynamic volume of the particle ($V_{\mathrm{H}}$), [8]. Effectively, the relaxation time is combined as these two

$$\begin{aligned} \tau_N &= \frac{\tau_0}{2}\sqrt{\pi\frac{kT}{KV}}e^{KV/kT}, \\ \tau_B &= \frac{3\eta V_{\mathrm{H}}}{kT}, \\ \frac{1}{\tau} &= \frac{1}{\tau_{\mathrm{B}}}+\frac{1}{\tau_{\mathrm{N}}}. \end{aligned} \tag{1}$$

One of the models describing the energy loss of MNPs under the influence of AMF is the Rosensweig model, which is expressed as

$$P = \frac{1}{2}\omega\mu_0\chi_0 H^2\frac{\omega\tau}{1+\omega^2\tau^2}, \tag{2}$$

where $\chi_0$ is magnetic susceptibility, $H_{\mathrm{ac}}$ and $f$ are amplitude and frequency of AMF and $\omega$ is angular frequency.

This model correlates MNP energy loss with some physical properties of MNPs and AMF frequency and amplitude [8].

In practical applications of MFH, MNPs tend to move from tumor to healthy tissue over time. In an example study, the effect of dynamic viscosity ($3\times10^{-5}\,\mathrm{Pa\,s}$) on particle concentration and particle velocity distributions in healthy and tumor tissue were examined numerically [9]. Cancerous cells and healthy tissue regions are represented as concentric circles and MNP injection point is center of inner circle. It was observed that MNPs transported from tumor region to the healthy tissue over time. Because AMF is applied to the entire area, MNPs undesirably heat healthy tissue after certain time. Therefore,

[1] Balikesir University, Faculty of Engineering, Department of Electrical and Electronics Engineering, 10463, Balikesir, Turkey, kucukdermenci@balikesir.edu.tr

https://doi.org/10.2478/jee-2022-0020, Print (till 2015) ISSN 1335-3632, On-line ISSN 1339-309X

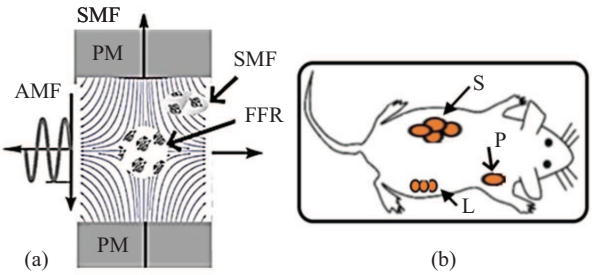


**Fig. 1.** (a) – Field free region formation by static magnetic field sources, (b) – schematic representation of test animal as target object

increasing the temperature of the tumor without damaging the healthy tissue surrounding the tumor emerges as a problem. Local focusing is necessary to ensure that heat is only increased at the target lesion site.

According to theoretical and experimental studies [10, 11] MNP behaviors under the influence of AMF can be changed with static magnetic field superposition. When static magnetic field sources are placed with two repelling poles face-to-face, this positioning creates static magnetic field free region at the center of the workspace and gradient zones at the corners, see Fig. 1(a). Thus, MNPs in the field free region can be freely oscillates while the entire region is under the influence of AMF. Conversely, the oscillations of MNPs outside the field free region is restricted or completely blocked by static magnetic field gradients.

In bioelectromagnetic applications, current-fed electromagnets [12] or permanent magnets [13] could be preferred as static magnetic field sources. Coils require power supplies and, in some cases, coolers. This makes experiment setups more complex and costly. Compared to coils, neodymium iron boron (NdFeB) magnets have higher magnetic flux density [14] and magnet-based experimental setups are less complex and relatively cost-effective compared to coil-containing setups.

Tasci *et al* [15] proposed a test setup with an static magnetic field source made of DC coils. These coils are on both sides of the AMF generating coil. The study showed that MNP oscillations can be controlled locally by the effect of static magnetic field gradient and field free region. Lu *et al* [16] used magnets to focus the heat on a specific region. With their setup, both magnetic particle imaging and MFH operations can be performed together. Ma *et al* [17] used NdFeB magnets as static magnetic field source. It is observed that the temperature rise of MNPs is limited when they are in the static magnetic field gradient. Gradient pattern mapping was not studied in detail in any of these studies.

A comparison between workspaces and target objects in the literature for MFH tests is shown in Tab. 1. Workspace is usually the internal volume of the helically shaped work coil. Test tubes containing ferrofluid or regional tumor masses in small animals can be considered as target objects. For in vitro testing, small test tubes or a long test tube containing MNP can be used as target object. A long test tube can have a length of 47.5 mm and an outer diameter of 9.6 mm. The field free region can be overlapped with parts of the long tube. If the tumor mass in the small animal is target object, it may have point-like, line-like or surface-like geometries as indicated by the letters $P$, $L$ and $S$, see Fig. 1(b).

Optimizing the distance between the static magnetic field sources and target object in the workspace may be necessary in different test setups. In this case, magnet arrays emerge as ideal candidates compared with coils and individual magnets. Halbach arrays are a permanent magnet configuration in which the magnetic field is maximum on one side and minimum on the other, see Fig. 2. This type of arrays increase the magnetic field intensity by 1.4 times compared to a standard magnetic array with the ability to orient magnetic field lines efficiently [18]. Halbach magnet arrays provide more remote intervention compared to other static magnetic field sources with their strong magnetic field generation properties. This allows for a localized flux concentration in the area of interest for operation. Correct positioning of dual array structure can create field free region in the workspace. In the light of the explanations above, the investigation of the usability of the magnetic field patterns formed by dual Halbach

**Table 1.** Comparison of workspaces and target objects in MFH experiment setup

| Features of workspace | Features of target object | Reference |
|---|---|---|
| radius $\approx 2$ cm, height $\approx 6$ cm, crossection of the workspace $\approx 24\,\mathrm{cm}^2$ | spherical plastic containers, $r \approx 0.2$ cm target area $\approx 0.126\,\mathrm{cm}^2$ | [15] |
| coil diameter = 3 cm | the two phantoms are located close to the heating zone of the coil (20 mm) | [17] |
| radius of the coil $\approx 5$ cm crosssection of the workspace $\approx 78.5$ cm | a test tube in the center of the coil, tube radius $\approx 0.5$ cm, target area $\approx 0.785\,\mathrm{cm}^2$ | [19] |
| coil diameter = 4 cm, length = 10 cm, crossection of the workspace $\approx 40\,\mathrm{cm}^2$ | spherical core with a radius of 4.9 mm | (20) |
| circle diameter = 90 mm, a square of. $56 \times 56$ mm$^2$ can be fitted into | target object can be a small test tube array, a long test tube or a small test animal | proposed study |

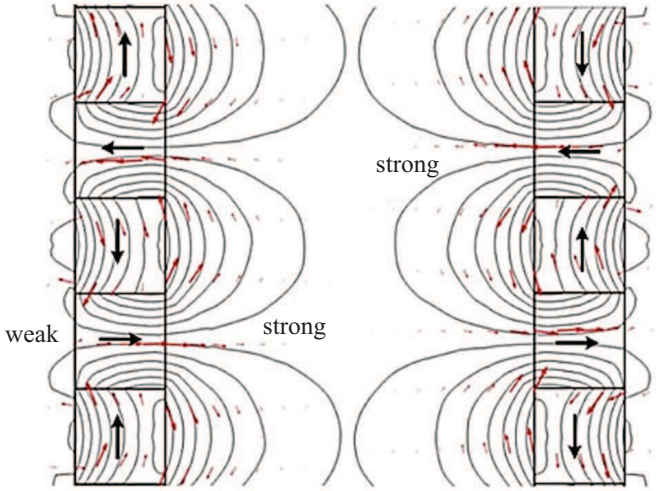


**Fig. 2.** Magnetic flux lines of dual Halbach array

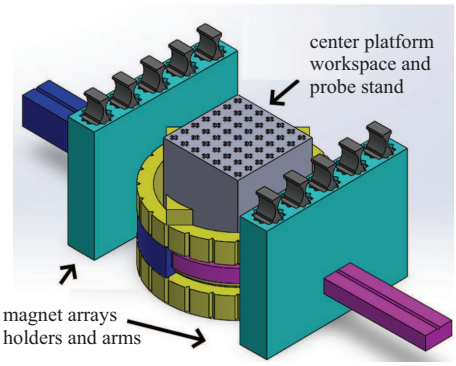


**Fig. 3.** Parts of the experiment platform

**Table 2.** Magnetization directions of array elements

| Left array $(x, y, z)$ | Right array $(x, y, z)$ |
|---|---|
| $(0, 1, 0)$ | $(0, -1, 0)$ |
| $(-1, 0, 0)$ | $(-1, 0, 0)$ |
| $(0, -1, 0)$ | $(0, 1, 0)$ |
| $(1, 0, 0)$ | $(1, 0, 0)$ |
| $(0, 1, 0)$ | $(0, -1, 0)$ |

array for MFH was examined for the first time in this study.

## 2 Materials and methods

Five N54 grade NdFeB magnets were used to construct the Halbach arrays. Each magnet has a volume of $10 \times 10 \times 40$ mm$^3$. Here, $B_r$ and $\mu_{recq}$ of magnets are 1.47 T and 1.05 T, respectively. Halbach arrays were created by rotating each magnet at an angle of 90°C from the previous one, see Tab. 2. The dual Halbach array poles are arranged so that the strong magnetic fields of the arrays face each other, Fig. 2. Further, $(d_1, d_2)$ are the distances between the center of gravity of the arrays and the origin of the workspace. Six cases were chosen to investigate the effect of dual Halbach array positions on field free region, see Tab. 3.

**Table 3.** Array locations on both sides

| Case | $(d_1, d_2)$ |
|---|---|
| 1 | $(-64, +64)$ |
| 2 | $(-69, +69)$ |
| 3 | $(-74, +74)$ |
| 4 | $(-79, +79)$ |
| 5 | $(-84, +84)$ |
| 6 | $(-89, +89)$ |

**Table 4.** Locations of array elements

| Left array (x, y, z) | Right array (x, y, z) |
|---|---|
| $(d_1, 42, 0)$ | $(d_2, 42, 0)$ |
| $(d_1, 21, 0)$ | $(d_2, 21, 0)$ |
| $(d_1, 0, 0)$ | $(d_2, 0, 0)$ |
| $(d_1, -21, 0)$ | $(d_2, -21, 0)$ |
| $(d_1, -42, 0)$ | $(d_2, -42, 0)$ |

### *2.1 Simulation medium*

A multi-physics simulation software (COMSOL® Multiphysics 5.6, COMSOL AB, Stockholm, Sweden) was used for modeling. The simulation medium consists of dual Halbach array and target object. Locations of array elements are presented in Tab. 4. The target object is a cylinder with a radius of 28 mm and a height of 56 mm. A test tube or a small test animal can be placed in this area for in vitro or in vivo applications, respectively.

### *2.2 Experiment setup*

Experiment setup consists of magnets, 3D-printed single magnet holders, magnet holders for five-element array, left and right arms, center platform and probe stand, see Fig. 3. Magnets are placed inside the single magnet holders. Then single magnet holders are inserted into array magnet holders. Five-element array magnet holders are attached to the arms. The array distances can be changed gradually by the help of arms. Holders, arms and center platform are connected together. Center platform keeps all system aligned and its center room is used for measuring. This room is a 90 mm diameter circle and a square of $56 \times 56\,\mathrm{mm}^2$ can be fitted into it. Probe stand is placed inside of this room.

The probe stand allows the measurement of magnetic flux density in the $x$ and $y$ directions ($B_\mathrm{x}$ and $B_\mathrm{y}$) from 49 points. Technical drawings of each part and information of 3D printing process can be found as a file in supplementary materials.

## 3 Results and discussion

### *3.1 Simulation results*

Color maps of magnetic flux density and arrow representations of flux lines for six different cases are shown in Fig. 4(a)–(f), respectively. When the array positions are close to the target object, the field free region is in a centrally focused dot-like form. It was observed that the field free region form became ellipse-like as the arrays moved away from the target object.

The MFH experiment conditions in the literature vary widely. For example, AMF intensity can range from 0.8 to 115 kA/m, [21]. To determine the field free region, an arbitrary cutoff must be chosen. Here limit value of static magnetic field is arbitrarily set to 20 G ($\approx 1.6$ kA/m). Contour lines are drawn at 20 G intervals and areas less than and equal 20 G can be considered as field free region for all cases. As seen in Fig. 5, field free regions ($B \leq 20$ G) are geometrically close to the elliptical surface area. Semi-major axis $a$ and semi-minor axis $b$ of field free regions were measured. $(a, b)$ are $(0.85, 0.7)$, $(1.15, 0.95)$ and $(2.1, 1.3)$ cm for cases 1–3, respectively. The equation $A = \pi ab$ gives the area of the ellipse. The surface areas are 1.87, 3.43 and $8.57\,\mathrm{cm}^2$ for cases 1–3 respectively. It is found that, if the magnet arrays come closer to the target object symmetrically, the field free region can focus on a tiny area. If the field free regions for cases 4–6 are considered as rectangular form, their height is taken as 5.3 cm. The width of the rectangles can be taken as the average of the center width and the upper side width. The center widths are 3.3, 4.1, 5.1 cm, edges are 2.2, 3.6, 4.7 cm and rectangle-like surface areas are 14.58, 20.41 and $25.97\,\mathrm{cm}^2$ for cases 4–6, respectively. It is found that,

**Table 5.** Point probe measurements

**Supplementary material**
Point probe measurements in simulation medium, technical drawings of each part and information of 3D printing process for experiment setup are available online at
https://docs.google.com/doc ument/d/1lWfWtoov9hdyQCW3tHoZWKPmjE8TpXb1/

| | | Case 1 | | | | | | | Case 2 | | | | | | | Case 3 | | | | | | | |
|---|---|---|---|---|---|---|---|---|---|---|---|---|---|---|---|---|---|---|---|---|---|---|---|
| B (G) | | $x$-axis probe position (mm) | | | | | | | $x$-axis probe position (mm) | | | | | | | $x$-axis probe position (mm) | | | | | | | |
| | | -24 | -16 | -8 | 0 | 8 | 16 | 24 | -24 | -16 | -8 | 0 | 8 | 16 | 24 | -24 | -16 | -8 | 0 | 8 | 16 | 24 |
| | 24 | 209 | 128 | 92 | 82 | 91 | 127 | 208 | 149 | 93 | 69 | 59 | 68 | 93 | 150 | 106 | 66 | 50 | 47 | 47 | 68 | 108 |
| $y$ | 16 | 209 | 129 | 79 | 67 | 78 | 120 | 219 | 145 | 89 | 59 | 48 | 57 | 84 | 150 | 104 | 66 | 44 | 38 | 44 | 65 | 109 |
| -axes | 8 | 192 | 113 | 55 | 40 | 55 | 102 | 192 | 136 | 81 | 39 | 25 | 39 | 73 | 133 | 96 | 57 | 29 | 20 | 29 | 51 | 95 |
| probe | 0 | 196 | 91 | 49 | 3 | 45 | 94 | 177 | 136 | 64 | 36 | 6 | 34 | 68 | 124 | 94 | 49 | 22 | 2 | 21 | 52 | 85 |
| pos. | -8 | 190 | 109 | 53 | 41 | 55 | 101 | 200 | 136 | 77 | 40 | 30 | 42 | 73 | 129 | 95 | 54 | 28 | 19 | 33 | 52 | 98 |
| (mm) | -16 | 218 | 126 | 76 | 69 | 78 | 119 | 204 | 150 | 88 | 54 | 50 | 60 | 82 | 146 | 107 | 65 | 39 | 36 | 42 | 61 | 105 |
| | -24 | 213 | 128 | 94 | 82 | 90 | 132 | 210 | 149 | 90 | 68 | 61 | 64 | 97 | 148 | 102 | 64 | 50 | 42 | 52 | 68 | 108 |
| | | Case 4 | | | | | | | Case 5 | | | | | | | Case 6 | | | | | | | |
| B (G) | | $x$-axis probe position (mm) | | | | | | | $x$-axis probe position (mm) | | | | | | | $x$-axis probe position (mm) | | | | | | | |
| | | -24 | -16 | -8 | 0 | 8 | 16 | 24 | -24 | -16 | -8 | 0 | 8 | 16 | 24 | -24 | -16 | -8 | 0 | 8 | 16 | 24 |
| | 24 | 77 | 51 | 41 | 36 | 39 | 49 | 74 | 56 | 37 | 29 | 23 | 29 | 36 | 53 | 42 | 29 | 24 | 18 | 21 | 27 | 38 |
| $y$ | 16 | 75 | 45 | 30 | 25 | 33 | 48 | 77 | 52 | 33 | 26 | 23 | 26 | 37 | 55 | 37 | 27 | 15 | 16 | 15 | 24 | 41 |
| -axes | 8 | 68 | 40 | 20 | 14 | 25 | 39 | 67 | 47 | 29 | 18 | 11 | 16 | 30 | 48 | 34 | 25 | 10 | 12 | 13 | 22 | 33 |
| probe | 0 | 69 | 38 | 16 | 2 | 20 | 35 | 60 | 51 | 24 | 16 | 4 | 16 | 26 | 46 | 39 | 21 | 9 | 5 | 11 | 23 | 34 |
| pos. | -8 | 67 | 42 | 23 | 13 | 23 | 37 | 66 | 46 | 32 | 19 | 10 | 19 | 28 | 49 | 33 | 23 | 11 | 8 | 14 | 23 | 36 |
| (mm) | -16 | 74 | 45 | 31 | 30 | 32 | 45 | 71 | 56 | 35 | 22 | 22 | 24 | 33 | 50 | 42 | 25 | 16 | 16 | 17 | 23 | 41 |
| | -24 | 76 | 47 | 38 | 35 | 35 | 49 | 78 | 57 | 37 | 30 | 28 | 28 | 35 | 53 | 38 | 30 | 24 | 17 | 22 | 31 | 39 |

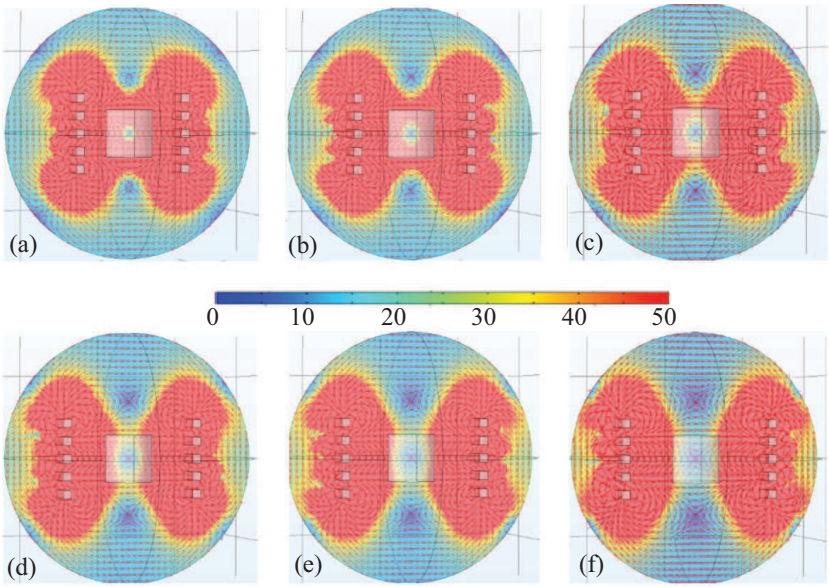


**Fig. 4.** Color maps and arrow representations for (a) – case 1, (b) – case 2, (c) – case 3, (d) – case 4, (e) – case 5 and (f) – case 6

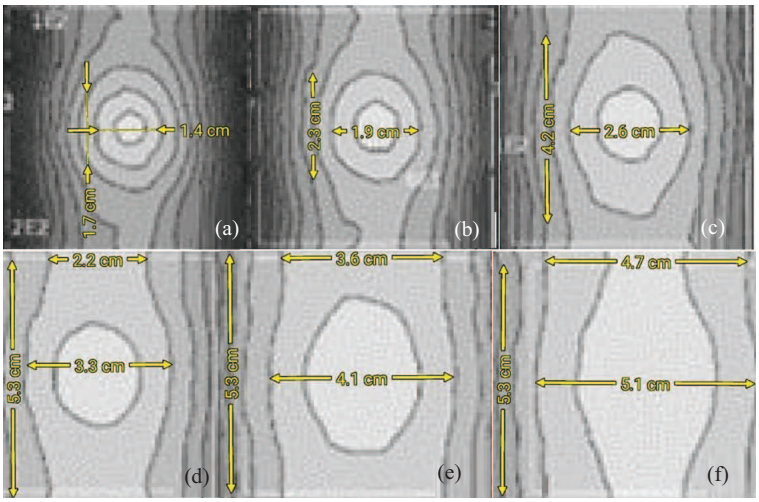


**Fig. 5.** Field free region contour plots and axis measurements for (a) – case 1, (b) – case 2, (c) – case 3, (d) – case 4, (e) – case 5 and (f) – Case 6

the field free region form broadens when the dual Halbach array moves aways from the target object. Among the resulting field free regions in these six cases, appropriate ones can be selected, taking into account target object s such as small test tubes, a long test tube or a small test animal.

As much as 49 measuring points were identified on the $x$ and $y$ axes at 8 mm intervals from $-24$ mm to 24 mm in the workspace. Point probe measurements of the static magnetic field for the simulation medium were generated for all cases. Related tables can be found as a file in the supplementary materials.

### *3.2 Experiment setup*

Point probe measurements were taken at the same probe positions as in the simulation. Magnetic flux measurements in the $x$ and $y$ directions ($B_\mathrm{x}$ and $B_\mathrm{y}$) were taken for all cases with WT10A commercial magnetic flux meter. The magnitude of magnetic flux density for every point was $B = \sqrt{B_\mathrm{x}^2 + B_\mathrm{y}^2}$. Measurements were repeated four times in a row and the average values were transferred to Tab. 5. The number of points forming the field free region (red-colored regions in Tab. 5, $B \leq 20\,\mathrm{G}$) are 1, 1, 3, 5, 9 and 17 for case 1–6, respectively. It is seen that point probe measurements in experiment setup give information about position and flux density levels of the field free regions.

### *3.3 Discussions*

Small deviations of point probe measurements between simulation medium and experiment setup may have various reasons. For instance, magnets are identical in simula-

tion medium but in real life they may not be exactly the same. Commercial flux meter measurements were done with hand and probe alignments cant be perfect as in the simulation. Some gaps should be added to the 3D printed objects for assembly. For example, the magnet edges should be set to 10 and 40 mm, while the room edges in the holder should be set to 10.3 and 40.3 mm (see supplementary materia). 3D printouts may differ from the ideal dimensions in the drawing. This can lead to inevitable alignment and measurement differences.

## 4 Conclusions

In this study, gradient pattern mapping produced by parametric position changes of a dual Halbach array for using in focused MFH tests was investigated for the first time. It is found that, symmetric displacements of a dual Halbach array can manipulate field free region form (changes its shape to rectangle-like and ellipse-like forms) and location (can be focused to center of the target object). Field free region structures were analyzed with color maps and arrow representations, axis measurements and area calculations from contour representations, point probe measurements and mappings of gradient patterns. The utilized system in this study could be used in real scenario if the specific conditions of each experiment are taken into account. For in vitro tests, field free region can be applied to test tubes in a periodic array or a long tube with horizontal positioning. For MFH test with small animals, field free region and target tissue overlap can be achieved by appropriate placement of the static magnetic field source and/or target object.

The obtained results provide data for in vitro and in vivo MFH tests performed prior to clinical trials. With the help of gradient pattern mapping, suitable field free regions for different tumor geometries can be determined. The ability to ablate a tumor of any possible geometry by moving the field free region over the tumor is important for future studies. This highlights the importance of adapting the position and shape of the field free region in MFH applications. In the future, designs may be considered to focus field free region with highly sensitive robotic devices for each patient's unique individual conditions.

## References


[1] K. El-Boubbou, "Magnetic iron oxide nanoparticles as drug carriers: preparation, conjugation and delivery", *Nanomedicine*, vol. 13, no. 8, pp. 929-952, doi: 10.2217/nnm-2017-0320 2018.

[2] M. Domenech, I. Marrero-Berrios, M. Torres-Lugo, and C. Rinaldi, "Lysosomal Membrane Permeabilization by Targeted Magnetic Nanoparticles in Alternating Magnetic Fields", *ACS Nano*, vol. 7, no. 6, pp. 5091-5101, doi: 10.1021/nn4007048 2013.

[3] C. S. S. R. Kumar, and F. Mohammad, "Magnetic nanomaterials for hyperthermia-based therapy and controlled drug delivery", *Adv. Drug Deliv. Rev*, vol. 63, no. 9, pp. 789-808, doi: 10.1016/j.addr.2011.03.008 2011.

[4] W. Tao, and *et al*, "Two-Dimensional Antimonene-Based Photonic Nanomedicine for Cancer Theranostics", *Adv. Mater*, vol. 30, no. 38, p. 1802061, doi: 10.1002/adma.201802061 2018.

[5] A. Attaluri, and *et al*, "Magnetic nanoparticle hyperthermia enhances radiation therapy: A study in mouse models of human prostate cancer", *Int. J. Hyperth*, vol. 31, no. 4, pp. 359-374, doi: 10.3109/02656736.2015.1005178 2015.

[6] D. Chang, and *et al*, "Biologically Targeted Magnetic Hyperthermia: Potential and Limitations", *Front. Pharmacol*, vol. 9, doi: 10.3389/fphar.2018.00831 2018.

[7] W. F. Brown, "Thermal Fluctuations of a Single-Domain Particle", *Phys. Rev*, vol. 130, no. 5, pp. 1677-1686, doi: 10.1103/PhysRev.130.1677 1963.

[8] R. E. Rosensweig, "Heating magnetic fluid with alternating magnetic field", *J. Magn. Magn. Mater*, vol. 252, pp. 370-374, doi: 10.1016/S0304-8853(02)00706-0 2002.

[9] B. Tigli, "Numerical Analysis Of The Distribution Of Nanoparticles In The Treatment Of Hyperthermia Of Tumors", , Gazi Üniversitesi, 2019.

[10] R. Dhavalikar, and C. Rinaldi, "Theoretical predictions for spatially-focused heating of magnetic nanoparticles guided by magnetic particle imaging field gradients", *J. Magn. Magn. Mater*, vol. 419, pp. 267-273, doi: 10.1016/j.jmmm.2016.06.038 2016.

[11] P. Cantillon-Murphy, L. L. Wald, E. Adalsteinsson, and M. Zahn, "Heating in the MRI environment due to superparamagnetic fluid suspensions in a rotating magnetic field", *J. Magn. Magn. Mater*, vol. 322, no. 6, pp. 727-733, doi: 10.1016/j.jmmm .2009.10.050 2010.

[12] J. L. Ristic-Djurovic, and *et al*, "Design and Optimization of Electromagnets for Biomedical Experiments With Static Magnetic and ELF Electromagnetic Fields", *IEEE Trans. Ind. Electron*, vol. 65, no. 6, pp. 4991-5000, doi: 10.1109/TIE.2017.2772158 2018.

[13] S. Huang, Z. H. Ren, S. Obruchkov, J. Gong, R. Dykstra, and W. Yu, "Portable Low-Cost MRI System Based on Permanent Magnets/Magnet Arrays", *Investig. Magn. Reson. Imaging*, vol. 23, no. 3, p. 179, doi: 10.13104/imri.2019.23.3.179 2019.

[14] Z. Li, and *et al*, "Constituting abrupt magnetic flux density change for power density improvement in electromagnetic energy harvesting", *Int. J. Mech. Sci*, vol. 198, p. 106363, doi: 10.1016/j.ijmecsci.2021.106363 2021.

[15] T. O. Tasci, I. Vargel, A. Arat, E. Guzel, P. Korkusuz, and E. Atalar, "Focused RF hyperthermia using magnetic fluids", *Med. Phys*, vol. 36, no. 5, pp. 1906-1912, doi: 10.1118/1.3106343 2009.

[16] Y. Lu, and *et al*, "Combining magnetic particle imaging and magnetic fluid hyperthermia for localized and image- guided treatment", *Int. J. Hyperth*, vol. 37, no. 3, pp. 141-154, doi: 10.1080/02656736.2020.1853252 2020.

[17] M. Ma, Y. Zhang, X. Shen, J. Xie, Y. Li, and N. Gu, "Targeted inductive heating of nanomagnets by a combination of alternating current (AC) and static magnetic fields", *Nano Res*, vol. 8, no. 2, pp. 600610, doi: 10.1007/s12274-015-0729-7 2015.

[18] D. L. Trumper, M. E. Williams, and T. H. Nguyen, "Magnet arrays for synchronous machines,¡—", *Conference Record of the IEEE Industry Applications Conference Twenty-Eighth IAS Annual Meeting*, pp. 9-18, doi: 10.1109/IAS..298897 1993.

[19] L. M. Bauer, S. F. Situ, M. A. Griswold, and A. C. S. Samia, "High-performance iron oxide nanoparticles for magnetic particle imaging guided hyperthermia (hMPI)", *Nanoscale*, vol. 8, no. 24, pp. 12162-12169, doi: 10.1039/C6NR01877G 2016.

[20] Q. Zhao, and *et al*, "Magnetic Nanoparticle-Based Hyperthermia for Head dnd Neck Cancer in Mouse Models", *Theranostics*, vol. 2, no. 1, pp. 113-121, doi: 10.7150/thno. 3854 2012.

[21] V. Vilas-Boas, F. Carvalho, and B. Espia, "Magnetic Hyperthermia for Cancer Treatment: Main Parameters Affecting the Outcome of In Vitro and In Vivo Studies", *Molecules*, vol. 25, no. 12, p. 2874, doi: 10.3390/molecules25122874 2020.


Received 1 January 2022